Supporting Information:

Interlayer Coupling in Twisted WSe$_2$/WS$_2$ Bilayer Heterostructures Revealed by Optical Spectroscopy

Kai Wang[1*], Bing Huang[1,2,3], Mengkun Tian[4], Frank Ceballos[5], Ming-Wei Lin[1], Masoud Mahjouri-Samani[1], Abdelaziz Boulesbaa[1], Alexander A. Puretzky[1], Christopher M. Rouleau[1], Mina Yoon[1], Hui Zhao[5], Kai Xiao[1], Gerd Duscher[4], David B. Geohegan[1*]

1.Center for Nanophase Materials Sciences, Oak Ridge National Laboratory, Oak Ridge, Tennessee 37831 USA

2. Beijing Computational Science Research Center, Beijing 100094, China

3. Department of Materials Science and Engineering, University of Utah, Salt Lake City, Utah 84112, USA

4. Department of Materials Science and Engineering, University of Tennessee, Knoxville, Tennessee 37996 USA

5.Department of Physics and Astronomy, The University of Kansas, Lawrence, Kansas, 66045 USA

* Correspondence should be addressed to <u>wangk@ornl.gov</u> and <u>geohegandb@ornl.gov</u>
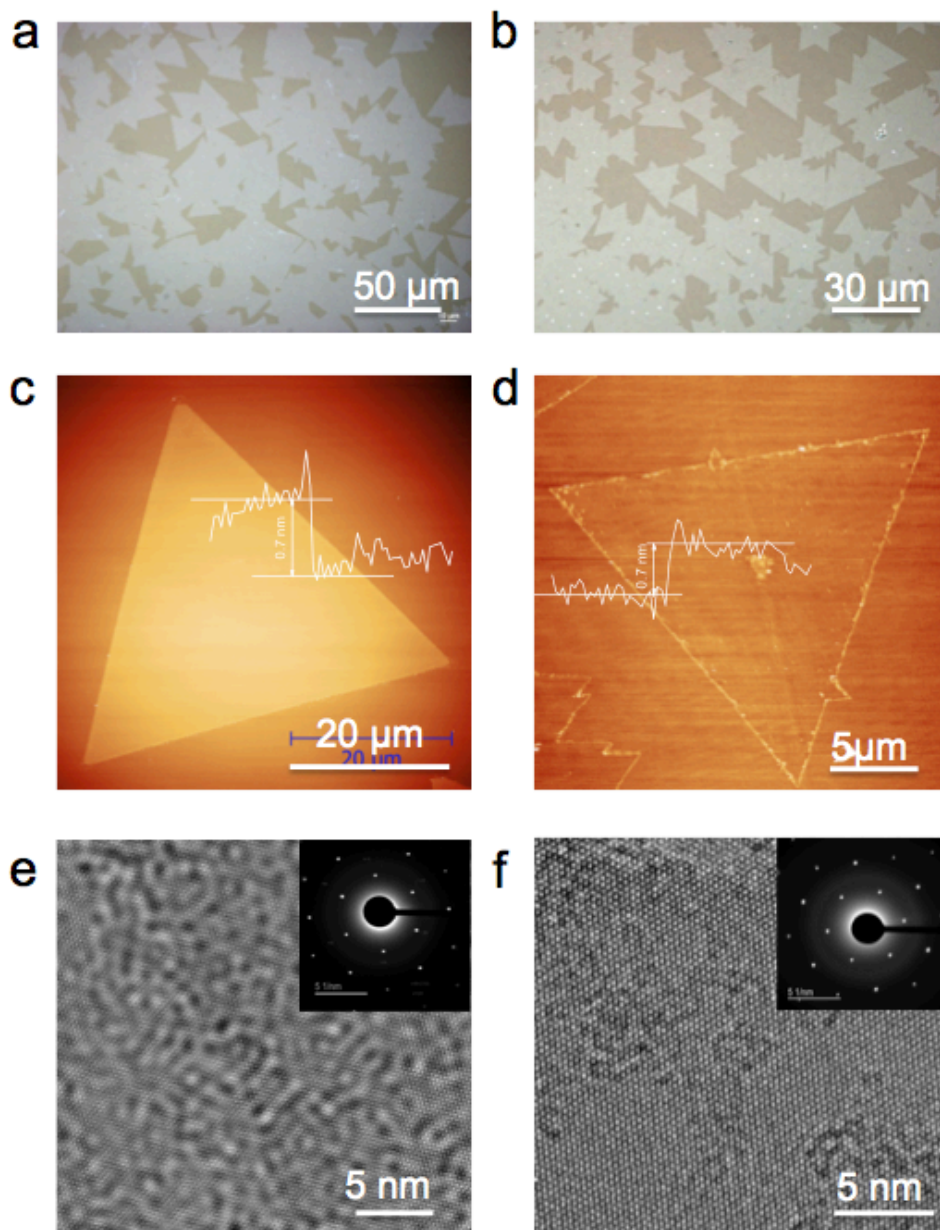
Content:

Figure S1. Structural analysis of WS$_2$ and WSe$_2$ 2D flakes directly grown on sapphire substrate by CVD. (a) and (b) optical microscope images of WS$_2$ and WSe$_2$ flakes. (c) and (d) AFM images and the edge profiles of ML WS$_2$ and WSe$_2$ triangular flake. (e) and (f) HRTEM images taken from ML WS$_2$ and WSe$_2$ flakes. Insets are the corresponding selected area electron diffraction (SEAD) patterns, respectively.
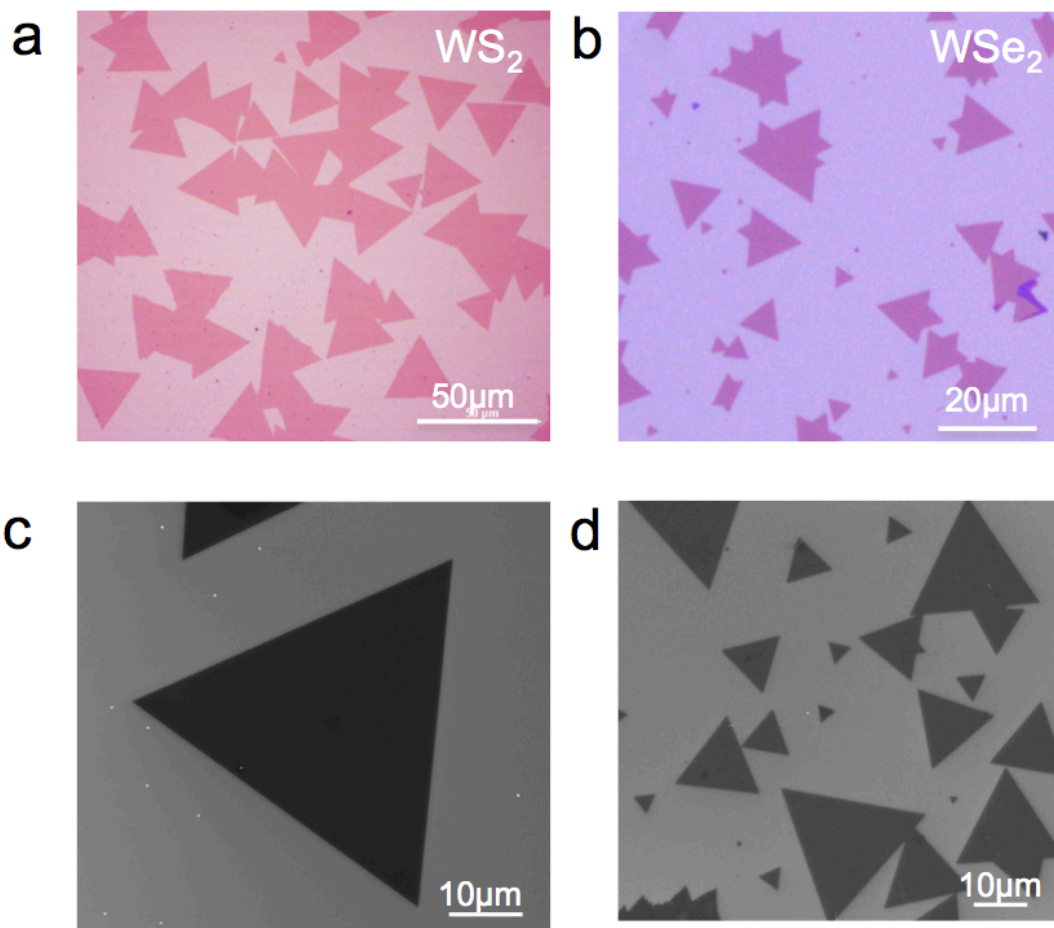
Figure S2 Size and shapes of WSe$_2$ and WS$_2$ 2D flakes directly grown on SiO$_2$/Si substrate by CVD. (a) and (b) optical microscope images of WS$_2$ and WSe$_2$ flakes. (c) and (d) SEM images of ML WS$_2$ and WSe$_2$ triangular flakes.
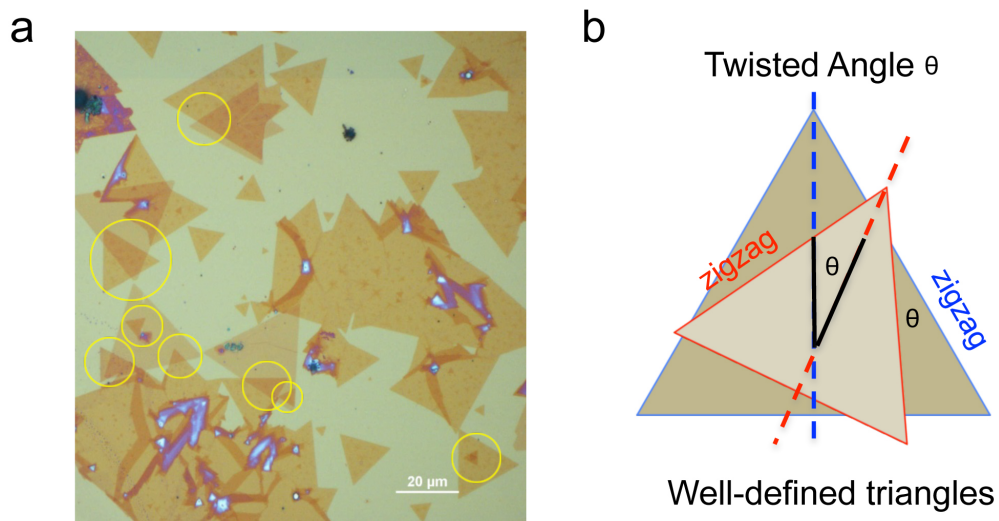
Figure S3. (a) Optical microscope image of stamped WSe_2/WS_2 BLs on SiO_2/Si substrate showing 8 different twist angles. (b) Schematic used to define the twist angles between the two layers. The perfect symmetry of as-transferred flakes before and after annealing allows us to precisely determine the twist angles using optical images.
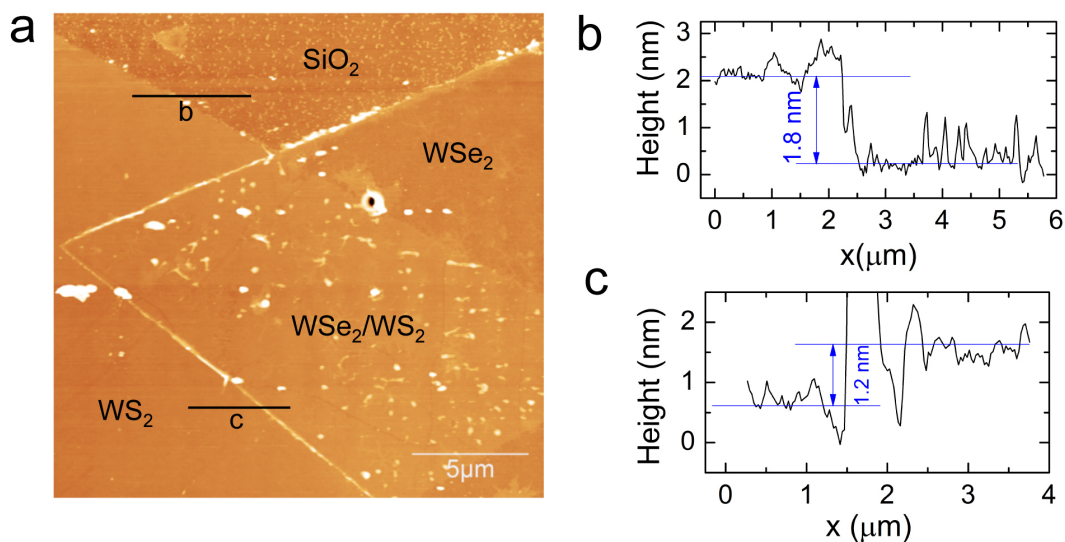

Figure S4. Influence of annealing on the distance between layers. (a) AFM image of a WSe_2/WS_2 BL before annealing. (b) and (c) Height profiles taken at the position of the black lines in (a). Without annealing, the measured height profiles of ML WS_2 on SiO_2 substrate and ML WSe_2 are 1.8 nm and 1.2 nm, respectively, which are larger than the thickness (~0.8 nm) of ML WS_2 measured after annealing. This indicates that the majority of any trapped water vapor or the polymer residue left on the sample is removed by annealing in Ar.
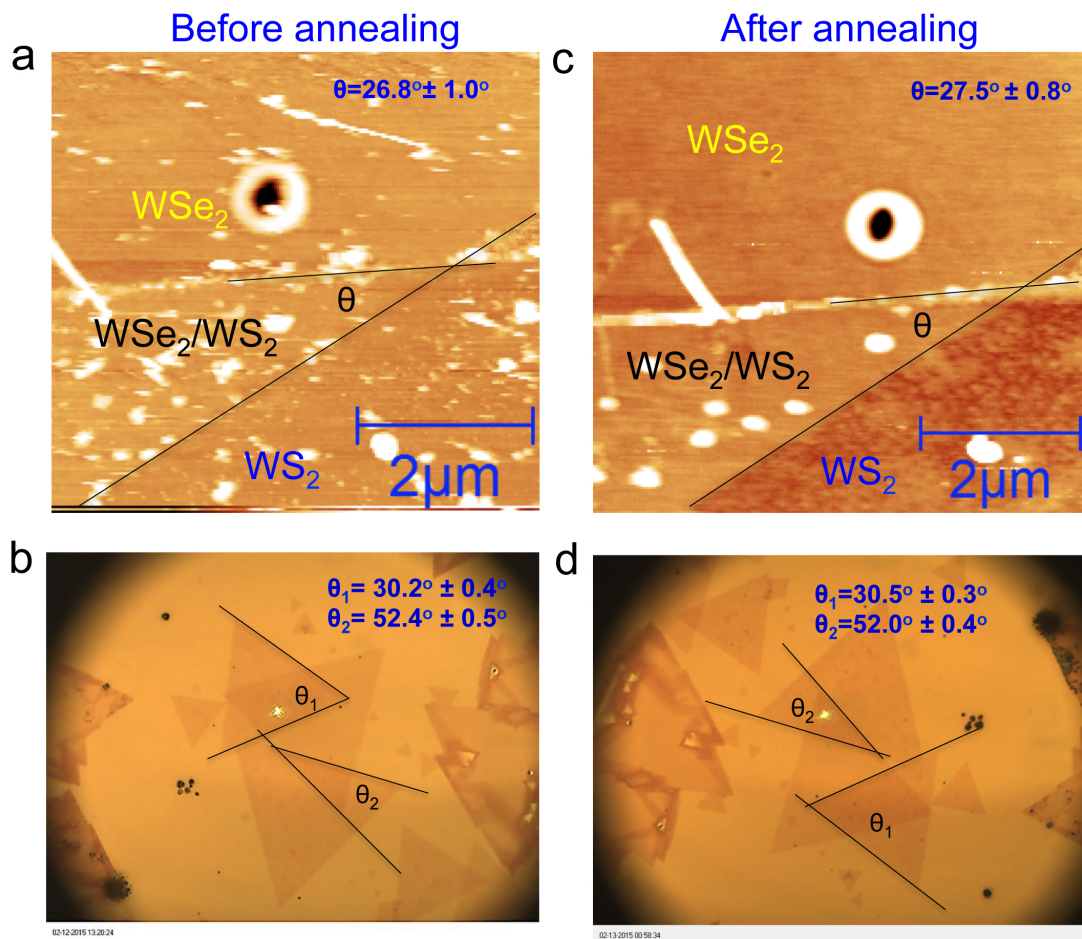
Figure S5. Influence of annealing on the twist angles. AFM images and optical microscope images of WSe$_2$/WS$_2$ bilayers before annealing ((a) and (b)) and after annealing ((c) and (d)). The twist angles change before and after annealing is within the experimental uncertainty of $\pm$ 0.5^o.
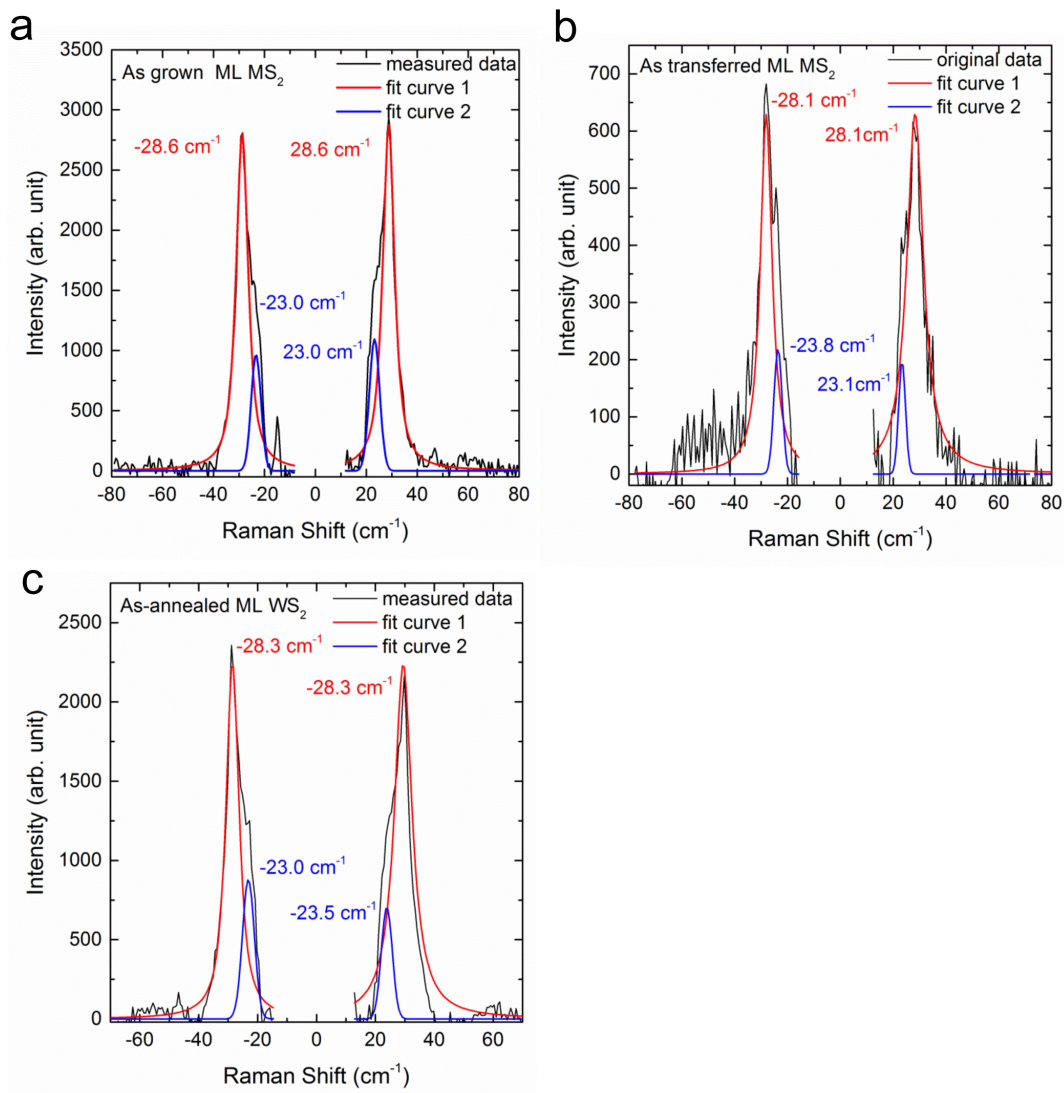
Figure S6. Low-frequency (LF) Raman spectra taken from ML WS₂ on SiO₂/Si substrates. (a) as-grown, (b) as-transferred, and (c) as-annealed. The black curve is the measured LF Raman spectrum after subtracting the background, which can be fitted by a main peak (in red) and a small peak (in blue).

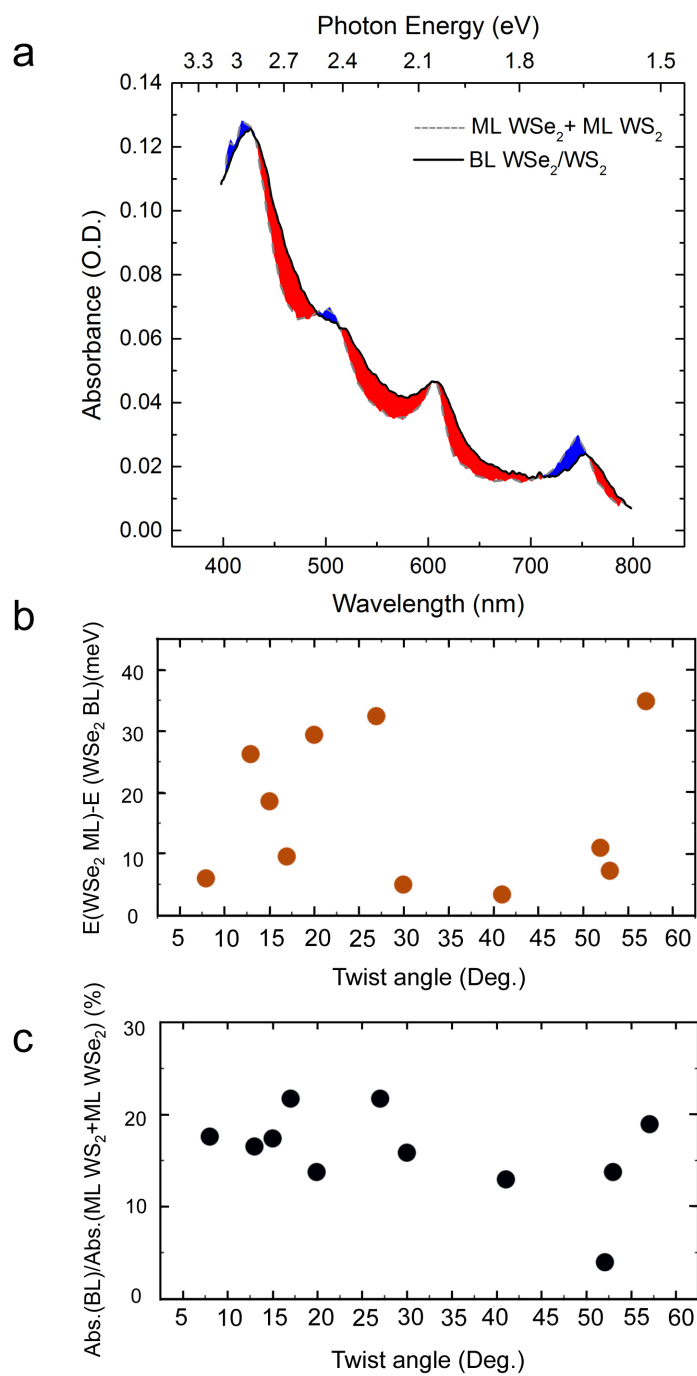**Figure S7. Absorption in WSe₂/WS₂ BL. (a)** WSe₂/WS₂ BL shows ~10 % enhancement in absorbance range of 400 nm~800 nm, as indicated by the red shaded regions. (b) Statistical analysis of the redshifts of the WSe₂ exciton A band in BL relative to that in ML, E(WSe₂ ML)-E (WSe₂ BL). (c) Ratio of absorbances, Abs.(BL)/Abs.(ML WS₂+ML WSe₂). Note that the absorbances were integrated from 570 nm (2.17 eV) to 800 nm (1.55 eV).
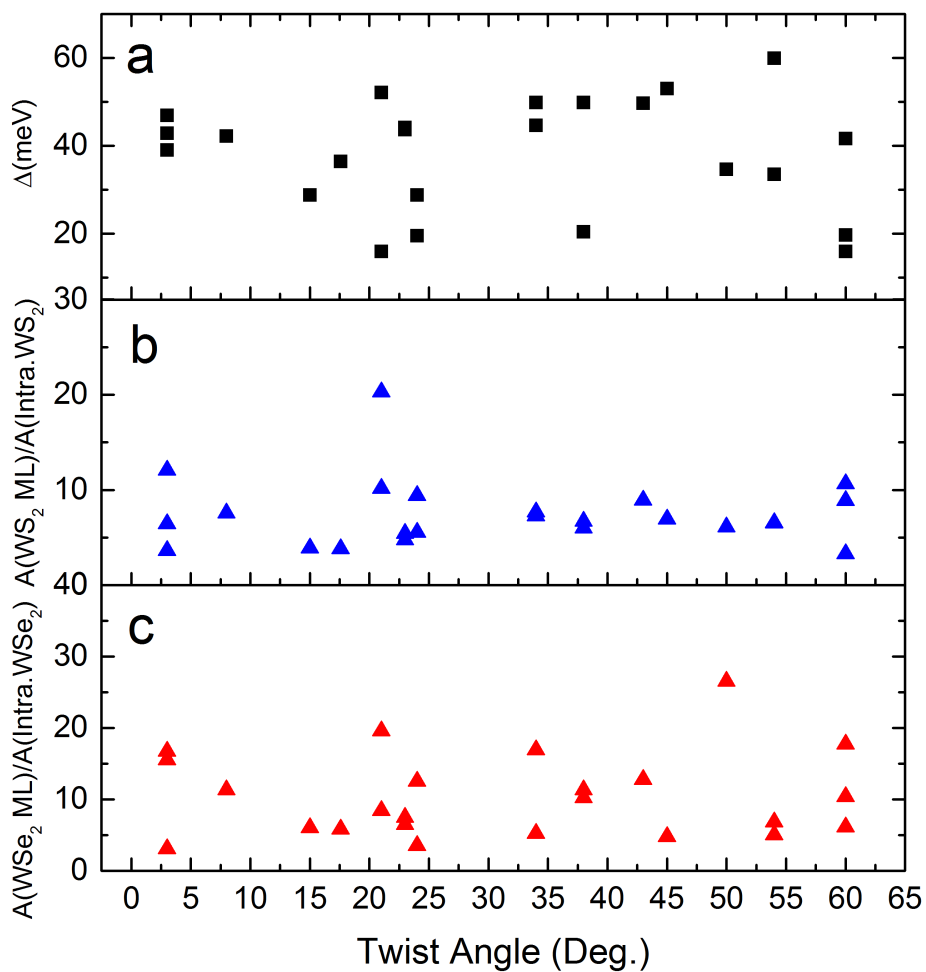
Figure S8. Statistical analysis of PL data for WSe$_2$/WS$_2$ BLs. (a) the redshift (Δ) of the WSe$_2$ exciton A band in BL relative to that in ML, E(WSe$_2$ ML)-E(WSe$_2$ BL), and the ratio of PL intensity: (b) A(WS$_2$ ML)/A(Intra.WS$_2$) for WS$_2$ and (c) A(WSe$_2$ ML)/A(Intra.WSe$_2$) for WSe$_2$, respectively. To determine the quenching magnitudes in PL intensity, we compared the integrated area under the spectra from 1.85 eV to 2.15 eV for WS$_2$ and from 1.5eV to 1.78 eV for WSe$_2$. No clear trends of the redshift and the magnitudes of intralayer PL quenching with the twist angle were observed.

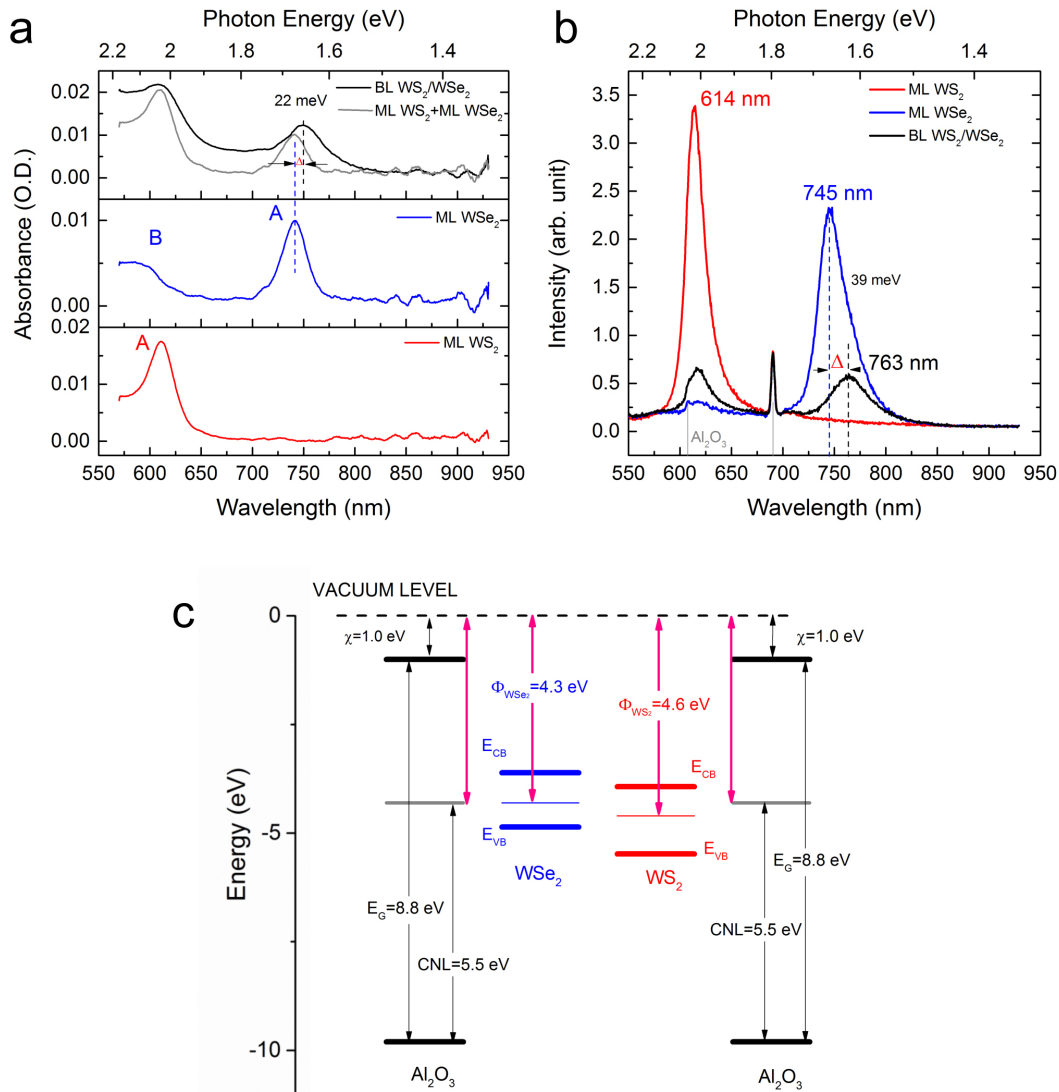**Figure S9. Light absorption and emission characteristics of WS$_2$/WSe$_2$ BLs on sapphire substrate and associated energy level diagram.** (a) Absorption and (b) photoluminescence spectra taken from ML WSe$_2$, ML WS$_2$ and WS$_2$/WSe$_2$ BLs on a sapphire substrate. (c) Schematic diagram of the energy level in Al$_2$O$_3$/ WSe$_2$/WS$_2$ and Al$_2$O$_3$/WS$_2$/WSe$_2$ sandwich structures. For the work function of ML WSe$_2$ and ML WS$_2$ (Φ_{WS_2} and Φ_{WSe_2}), we use the values of 4.6 eV and 4.3 eV [Britnell, *et al*. Science, 340, 1311 (2013)]; for the bandgap of WSe$_2$ and WS$_2$, we use the calculated data from the literature [Kang, *et al*. Appl. Phys. Lett, 102, 012111 (2013)]. The electron affinity (EA), band gap (Eg), and charge neutrality level (CNL) of Al$_2$O$_3$, were adapted from the literature [Pecock, *et al*. J. Appl. Phys, 92, 4712 (2002)].
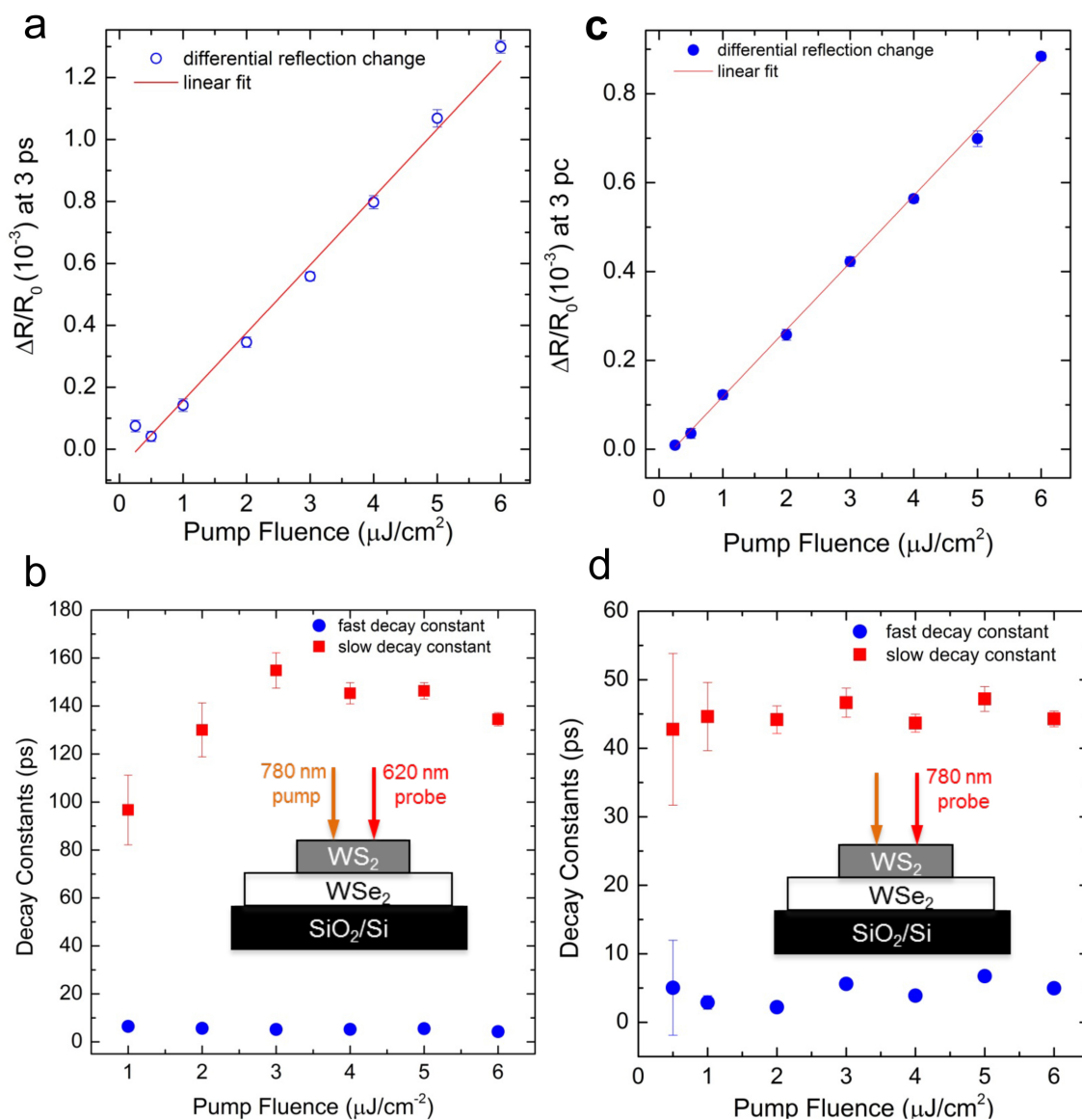
Figure S10. Pump-fluence-dependent differential reflectance and fitted decay *time* constants. (a) and (b) are collected using a 780 nm pump wavelength and a 620-nm probe pulse.(c) and (d) are collected with a 620 nm pump and a 780-nm probe pulse. Insets of (b) and (d) illustrate the corresponding pump-probe configurations.
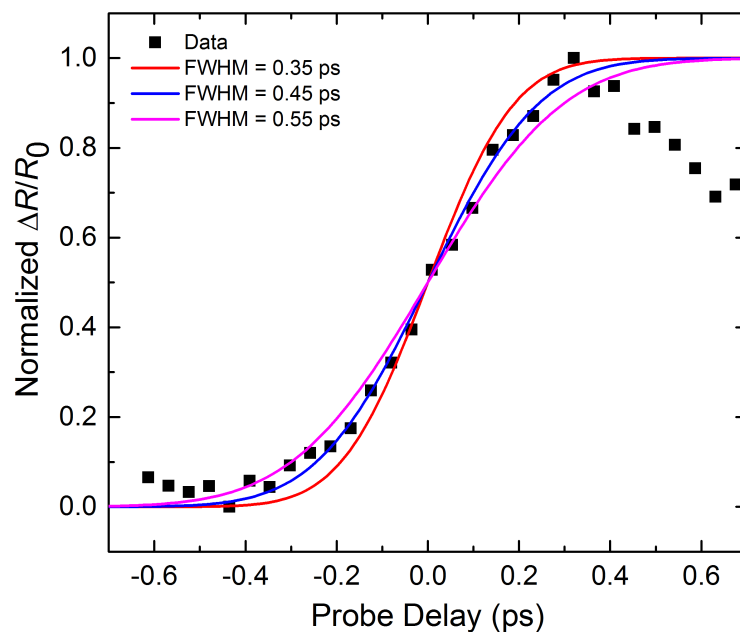
Figure S11. Instrument response determination for femtosecond transient absorption spectroscopy. Assuming that the response of the sample is instantaneous and the pump and probe pulses are infinitely narrow, $\Delta R/R_0$ should be a step function that jumps at zero delay (ignoring decay of the signal). Here the width of the cross correlation of the pump and probe pulses is determined to be ~450 fs. That translates to pulse widths of 0.32 ps for each pulse (FWHM intensity), using 0.45/1.414. Since the sample response cannot be instantaneous, this is actually the upper limit of the pulse width.
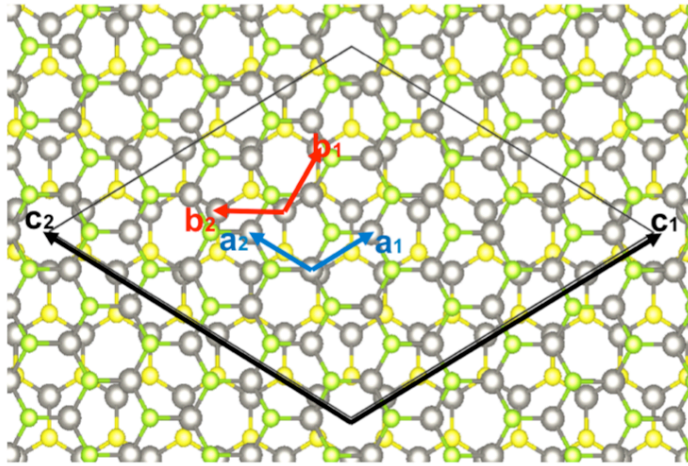
Figure S12. Schematics of a WSe$_2$/WS$_2$ supercell. WSe$_2$/WS$_2$ supercell is hexagonal with a primitive lattice vector $\vec{C} = n_1\vec{a_1} + n_2\vec{a_2} = (1 + \varepsilon)\theta(n_1\vec{b_1} + n_2\vec{b_2})$, where $\vec{a_1}$ and $\vec{a_2}$ are the lattice vectors of WSe$_2$, $\vec{b_1}$ and $\vec{b_2}$ are the lattice vectors of WS$_2$, and θ is the twist angle between WS$_2$ and WSe$_2$ layers.
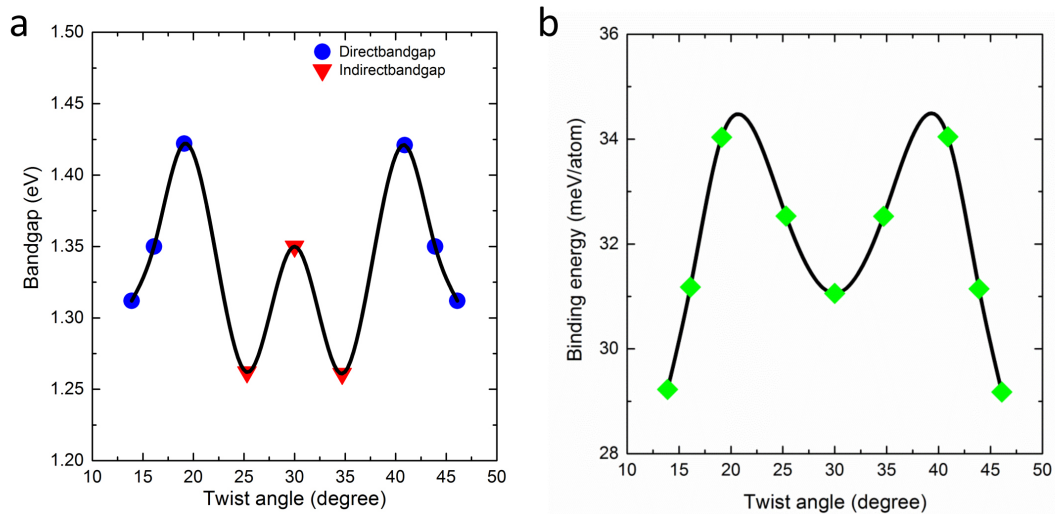

Figure S13. Band Structure calculations of WSe$_2$/WS$_2$ by PBE+vdW. (a) The DFT-calculated electronic band gap of a WSe$_2$/WS$_2$ heterojunction as a function of twist angle. (b) The DFT-calculated (including van de Waals interactions) binding energy of WSe$_2$/WS$_2$ heterojunction as a function of twist angle.
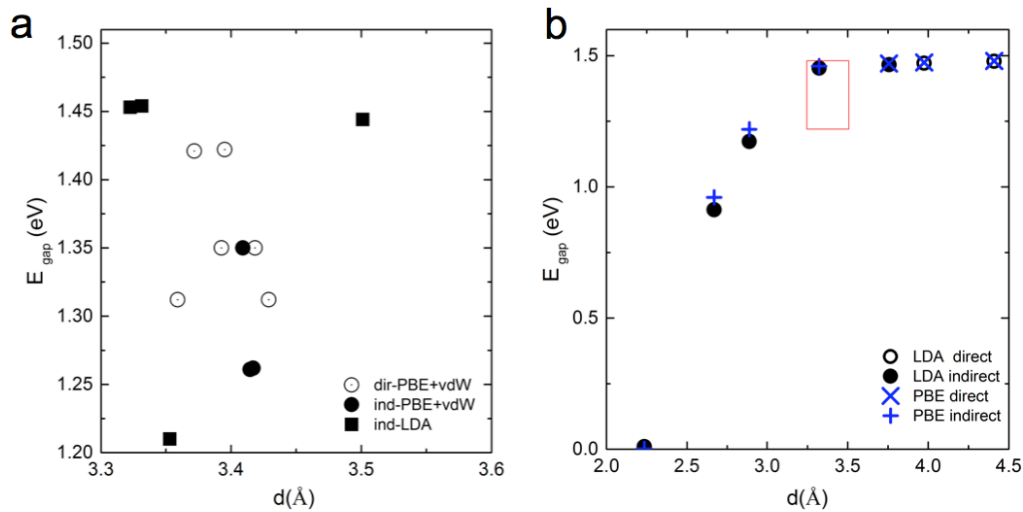
Figure S14 (a) Energy band gaps of structures optimized by either LDA or PBE+vdW functionals, where d is the optimized interlayer spacing of various twist angle structures considered in the study. Types of band gaps (indirect vs. direct) are indicated by the types of data points. (b) Energy band gaps of structures optimized by either LDA or PBE+vdW functionals. Types of band gaps (indirect vs. direct) are indicated by the types of data points.

Figure S14a presents energy gaps and their indirect/direct characteristics of structures fully optimized either by LDA or PBE+vdW. The plot compiles all the energy gaps obtained for the structures considered at various twist angles in terms of their interlayer spacing, d, optimized from the calculations. It clearly shows that direct-gap structures predicted by PBE+vdW are inconsistent with LDA predictions, that is, the PBE-predicted twist angles that indicate a direct band gap can be indirect using LDA and vice versa.

We reveal that interlayer spacing is the most prominent factor in determining energy gaps as well as their characteristics. For example, **Figure S14b** shows electronic energy gaps obtained for a BL structure at 19.1° twist angle for different interlayer spacing. Here the two layers were rigidly translated at different d without allowing a structural relaxation that is strongly affected by the choice of functionals. By this procedure we focus only on the effect of functionals in the electronic structures to draw a general conclusion on the correlation between interlayer distance and electronic structures. For both functionals, we find indirect to direct band gap transitions as interlayer distance increases. The non-

interacting regions clearly show direct band gaps, becoming indirect once the layers strongly interact with each other. However the exact transition point can be slightly different for different atomistic orientations between the layers. The region highlighted by red box is the range from Figure **S14a**, where the strength of the interlayer interaction lies in between non-interacting and strongly interacting. This is the region where the characteristics of the bands can be very easily changed depending on local orbital interactions. Here, the change in the local orbital interaction is so subtle that it is very difficult to deterministically predict direct-gap configurations. This finding is qualitatively consistent with the experimental data showing different PL band shifts even for the same twist angle. Moreover, depending on the experimental synthesis and processing conditions the interlayer distance may change slightly, which could introduce an excitonic peak if the layers are weakly coupled.